Stochastic 3D microstructure modeling of anodes in lithium-ion batteries with a particular focus on local heterogeneity

Benedikt Prifling[a,*], Marten Ademmer[a], Fabian Single[b], Oleg Benevolenski[b], André Hilger[c], Markus Osenberg[d], Ingo Manke[c], Volker Schmidt[a]

[a]*Institute of Stochastics, Ulm University, 89069 Ulm, Germany*
[b]*SGL Carbon GmbH, 86405 Meitingen, Germany*
[c]*Institute of Applied Materials, Helmholtz-Zentrum Berlin fÃ¼r Materialien und Energie, 14109 Berlin, Germany*
[d]*Department of Materials Science and Technology, TU Berlin, 10623 Berlin, Germany*

Abstract

Lithium-ion batteries can be considered as one of the most important energy storing devices. To satisfy the rapidly growing demand for higher energy densities, as for example required by automotive applications, the optimization of the electrode morphology is an important goal in battery research since it is well known that the 3D microstructure of anodes and cathodes has a significant impact on the resulting performance of the battery. A promising approach is called virtual materials testing, where stochastic 3D microstructure models are used to generate a wide range of virtual but realistic electrode morphologies as structural input for spatially-resolved numerical simulations of effective electrochemical properties. This beneficial combination allows to derive microstructure-property relationships just at the cost of computer simulations. The present paper introduces a novel parametric stochastic 3D microstructure model based on random fields that is calibrated to tomographic image data of six graphite anodes. The model is validated by comparing geometrical characteristics and effective tortuosity, which significantly influences the electrochemical behaviour of battery electrodes, computed for tomographic and simulated image data, respectively. A particular focus is put on local heterogeneity, which is quantitatively accessed by computing local distributions of certain microstructure-dependent descriptors.

Keywords: Stochastic microstructure modeling, Anode, Lithium-ion battery, Effective tortuosity, Local heterogeneity

---

1. Introduction

Due to their low self discharge rate, outstanding energy density and high power density, lithium-ion batteries are widely used in a broad spectrum of applications ranging from a variety of mobile electronic devices to electric vehicles. Thus, they can be considered as the most important technology for storing electrical energy currently used on an industrial scale [1, 2, 3]. Nevertheless, due to the fast growing demand for lithium-ion batteries, this promising technology has to fulfill permanently growing requirements, which is one of the reasons why the development of batteries

---

[*] Corresponding author. Email: benedikt.prifling@uni-ulm.de. Phone: +49 731 50 - 23555. Fax: +49 731 50 - 23649.

with optimized electrochemical performance is an essential objective of state of the art battery research [4, 5, 6, 7]. Further improvements of energy density, cycling stability and other key electrochemical characteristics can be achieved by the development of new materials as well as by enhancing electrodes consisting of materials which already exist [8, 9]. The latter can be realized, for example, by adapting the three-dimensional microstructure since it is well known that the 3D morphology of anodes as well cathodes is crucial for the resulting functionality of the battery [10, 11, 12, 13, 14, 15]. More precisely, the 3D microstructure of battery electrodes and thus their performance is significantly influenced by the underlying manufacturing process [16], which among others consists of mixing [17, 18], drying [17] and calendering [19, 20, 21].

Theoretical models of electrochemical cells enable quantitative insights into the nature of such interdependencies. In particular, these models allow a physics-based description of transport in each phase of the system [22]. This includes the solid phase of each electrode and the corresponding pores that are filled with liquid electrolyte. However, microstructure resolved battery simulations are computationally expensive and, therefore, require representative 3D structures. Such structures can be provided by tomographic 3D imaging of of real electrodes. Alternatively, they can also be generated with computational and analytical methods. However, in each case, the computational complexity of electrochemical simulations necessitates the use of a relatively small simulation domain. This forces the question, whether a given sample of this size, real or virtually generated, is representative to the required degree. The structures of typical electrode materials, especially graphite anodes, exhibit local heterogeneities which further complicate this issue. Nonetheless, virtually generated structures must exhibit heterogeneities similar to their real counterparts. Otherwise, electrochemical simulations will not predict comparable performance between the real and virtually generated structures in a statistically consistent way. Besides the overall morphology of battery electrodes, their local heterogeneity is an important influencing factor and can lead to cell overpotential, capacity fade and even complete failure of the cell [23, 24, 25]. These effects are especially pronounced at large overall current densities. Among others, effective tortuosity [26], degradation mechanisms [27], lithium-plating [28], electronic impedance [29] can strongly vary on local scale. In [30] it has been shown that 24 identically appearing cells show a very different behaviour after 600 cycles. This is in agreement with the results obtained in [31], where two cathodes with the same material composition and manufacturing process exhibited different microstructures after cyclic aging. Thus, a deeper understanding of the 3D morphology - both, on global and local scales, of anodes and cathodes and its dependency on manufacturing parameters is an important step for the design of battery electrodes with optimized properties.

Using parametric stochastic 3D microstructure models, the complex morphology of battery electrodes can be represented by a small number of model parameters, see [32, 33] for models calibrated to tomographic image data of cathodes and [34, 35] for anode models. Furthermore, they allow for an approach called virtual materials testing where a large number of virtual but realistic 3D microstructures is generated by systematic variations of the model parameters. In combination with spatially-resolved numerical simulations of effective properties, microstructure-property relationships can be derived just at the cost of computer simulations [36, 37, 38, 39, 40].
In addition, stochastic 3D microstructure models can be used to accelerate the design of battery electrodes made of a given electrode material by optimizing the effective properties of the electrode.

To this aim, only few electrodes with different manufacturing parameters need to be produced, e.g. with different levels of compaction. After calibrating one and the same type of a parametric model to these samples, the relationship between the manufacturing parameters and the parameters of the model can be revealed by regression analysis [32, 36, 41]. This relationship can be used to generate numerous 3D microstructures, which correspond to samples produced with further specifications of the manufacturing parameters. In this way, the number of samples that has to be manufactured can be reduced significantly. At the same time, manufacturing parameters, which optimize the effective properties of the electrode can be identified computationally.

The rest of this paper is organized as follows. In Section 2, we describe six graphite anodes, their preparation as well as the tomographic imaging procedure. Afterwards, several quantities for characterizing 3D microstructures are described in Section 3. They are used in Section 4 which deals with two different random set models based on χ^2-random fields, their calibration to tomographic image data and the validation of those models, where a particular focus is put on local heterogeneities and effective tortuosity. Section 5 concludes the paper with a short summary of the results as well as an outlook to possible future research.

2. Materials and imaging

2.1. Materials

Graphite anode electrodes were prepared at room temperature by mixing of at least 97 weight per cent of graphite powder with binder and further additives in water. Three different graphites were used (some commercially available as well as produced by SGL Carbon GmbH) further denoted as A, B and C types. The slurry was prepared by mixing the above-mentioned materials with distilled water in ratio 1:1 in weight. The process took place in a Speedmixer (DAC 250 SP, produced by Hausschild Engineering) in four steps, each taking about 2.5 minutes. The homogeneous slurry was coated on approximately 75 µm thick polyester film (Hostaphan RN, produced by Mitsubishi Polyester Film GmbH) with a table coater Coatmaster 510 D (produced by Erichsen) and dried at ambient conditions over a time of 30 minutes. The dry specimens were calendered to achieve two different densification degrees: electrodes with density of about $1.43\,\mathrm{g\,cm^{-3}}$ (indexed with 1, e.g. A1) and $1.63\,\mathrm{g\,cm^{-3}}$ (indexed with 2, e.g. A2) and an average layer thickness of about 80 µm. Thus, six different graphite anodes, denoted by A1, A2, B1, B2, C1, and C2 in total are considered in this paper.

2.2. Tomographic imaging procedure

The synchrotron tomography measurements have been conducted at the imaging beamline P05 which is operated by the Helmholtz-Zentrum Geesthacht (HZG) at the PETRA III storage ring (DESY) [42, 43]. The synchrotron beam was generated with an undulator (2 m in length) and monochromatized with a double crystal monochromator to an energy of 10 keV. After transmitting the sample, the monochromatic X-rays were transformed into visible light with a $\mathsf{CdWO_4}$ scintillator. The optical set-up provided a 10 times magnification and the image was detected with a CMOS camera “CMOSIS CMV 20000” with 5120 × 3840 pixels. A $3.29 \times 2.47\,\mathrm{mm}^2$ field of view was captured with a pixel size of 642 nm. For each tomography, 2001 radiograms over an angular range of 180° were captured with an exposure time of 600 ms. For the data processing and reconstruction Matlab based routines were used. The tomographic reconstruction was performed with the ASTRA toolbox [44, 45]. The voxel size of the reconstructed 3D image data is given by 642 nm. The resulting 3D grayscale images have been binarized using a global threshold [46], which has been determined such that the volume fraction of the solid phase computed from tomographic image data matches the volume fraction of the solid phase, which can be computed from material composition. The size of the sampling window is given by $1400 \times 1400 \times 79$ voxels for each sample.

3. Microstructure descriptors

This section deals with the description of characteristics that are used in Section 4 to quantify the goodness of fit of the stochastic 3D microstructure models proposed in the present paper. Namely, the 3D microstructure of the solid phase consisting of active material, binder and conductive additives will be modeled by a stationary and isotropic random closed set $\Xi_1 \subset \mathbb{R}^3$ [47]. The complement of the solid phase is given by the pore space, which is modeled by $\Xi_0 = \mathsf{cl}(\Xi_1^{\mathsf{C}})$, where $\mathsf{cl}(\Xi)$ and Ξ^{C} denote the topological closure and the complement of a subset $\Xi \subset \mathbb{R}^3$, respectively.

3.1. Volume fraction

To begin with, we consider the volume fraction of the solid phase, denoted by $\varepsilon_1 \in [0,1]$, which is defined as the mean value $\varepsilon_1 = \mathbb{E}\nu_3(\Xi_1 \cap [0,1]^3)$, where ν_3 denotes the three-dimensional Lebesgue measure. This quantity can be easily estimated from 3D image data by the point-count method, which is described in [48]. Obviously, the porosity ε_0, i.e. the volume fraction of the pore space Ξ_0, is given by $\varepsilon_0 = 1 - \varepsilon_1$.

3.2. Specific surface area

Next, we consider the specific surface area A of the solid phase, which equals the specific surface area of the pore space. Specific surface area is obtained by dividing the total surface area by the volume of the sampling window. The surface area has been estimated from 3D image data by differently weighted local $2 \times 2 \times 2$ voxel configurations using the weights proposed in [49].

3.3. Mean geodesic tortuosity

A further characteristic, which has turned out to influence transport properties [37], is the mean geodesic tortuosity, denoted by τ^{geo}. It is a purely geometrical quantity in contrast to effective tortuosity, which will be defined later on, see Section 3.7. For a comprehensive overview of different concepts of tortuosity, the reader is referred to [50, 51, 52]. The quantity τ^{geo} is the mean value of the distribution of minimal path lengths through a predefined phase from a starting plane to a target plane, divided by the distance of both planes. In the present paper, this quantity will be computed in z-direction, which in our case corresponds to the main direction of electrical and ionic transport. This direction is also known as through-plane direction. More precisely, the separator is chosen as starting plane and the current collector as target plane. The computation of shortest paths is carried out by means of Dijkstra's algorithm [53]. A formal definition of mean geodesic tortuosity within the framework of random closed sets can be found in [54].

3.4. *Chord length distribution*

Another important microstructure descriptor is the so-called chord length distribution [55, 56]. For simplicity, we do not consider chord lengths with respect to arbitrary directions, but only in $z-$direction, since we are restricting ourselves to isotropic random closed sets. The chord length distribution of a random closed set Ξ in z-direction can now be defined as the distribution of length of a line segment chosen at random in $\Xi \cap \ell$ where ℓ denotes the z-axis. The mean chord length of the random closed set Ξ_i is denoted by Cl_i. For further information regarding chord length distributions, the reader is referred to [48, 57, 58].

3.5. *Two-point coverage probability function*

Moreover, a further possibility to quantify the morphology of porous media is given by the so-called two-point coverage probability function $C_{i,j} : [0, \infty) \to [0, 1]$ with $i, j \in \{0, 1\}$, which is defined by

$$C_{i,j}(r) = \mathbb{P}(t \in \Xi_i, t + h \in \Xi_j)\,, \tag{1}$$

where $\|h\| = r$ and $\|h\|$ denotes the length of vector $h \in \mathbb{R}^3$ [48, 59]. In the present paper, the two-point coverage probability functions considered in (1) only depend on the distance r between the two points t and $t + h$ since Ξ_0 and Ξ_1 are both stationary and isotropic random closed sets. Note that $C_{i,i}(0) = \varepsilon_i$ for $i \in \{0, 1\}$ and $C_{i,i}(r) = 1-2\varepsilon_j+C_{j,j}(r)$ for $i \neq j$. In order to estimate $C_{i,j}$ from 3D tomographic image data, we use the Fourier-based method described in [58]. Furthermore, note that sometimes the notion covariance function is used for $C_{i,j}$ [55, 56]. In the case of estimating this characteristic from tomographic image data, one can typically observe that the value of $C_{i,j}(r)$ approaches $\varepsilon_i \cdot \varepsilon_j$ for large distances r, which implies that there is no correlation between two points far apart from each other. This quantity will play a major role in Section 4, when calibrating the random set models to tomographic image data.

3.6. *Constrictivity*

Last, but not least, a transport-relevant geometrical quantity is the constrictivity $\beta \in [0, 1]$, introduced in [60]. This characteristic allows us to quantify the strength of bottleneck effects, which turned out to strongly influence effective properties [39, 61]. In order to formally define constrictivity, we first have to introduce the notions of the continuous phase size distribution (CPSD) and the concept of simulated mercury intrusion porosimetry (MIP), where both characteristics are computed with respect to a predefined phase. The normalized continuous phase size distribution is a function $\mathsf{CPSD} : [0, \infty) \to [0, 1]$, where the value $\mathsf{CPSD}(r)$ is defined as the volume fraction of that part of the predefined phase, which can be filled using potentially overlapping balls with a given radius r such that these balls are completely contained in considered phase. Since $\mathsf{CPSD}(r)$ can also be expressed by a morphological opening using a ball with radius r as structuring element, this characteristic is also called opening size distribution [55, 56]. The radius for which the normalized continuous phase size distribution equals 0.5 is denoted by r_{max}. In contrast to the CPSD, simulated mercury intrusion porosimetry $\mathsf{MIP} : [0, \infty) \to [0, 1]$ is a direction-dependent function that contains additional information on the presence of bottlenecks and the connectedness of the considered phase. More precisely, the value $\mathsf{MIP}(r)$ is defined as the volume fraction of that part of the predefined phase which can be covered by an intrusion from a certain direction of (potentially overlapping) spheres with radius r, being completely contained in that phase. Analogously to r_{max}, the radius r_{min} is given by the radius for which the normalized MIP equals 0.5. By intruding the phase under consideration from a certain direction, MIP is decreasing faster compared to CPSD, which implies that $r_{\mathsf{min}} \leq r_{\mathsf{max}}$. Constrictivity is now defined as $\beta = (\frac{r_{\mathsf{min}}}{r_{\mathsf{max}}})^2$, where a value of β close to one indicates that there are almost no constrictions within the predefined phase. If β is close to zero, strong bottlenecks occur, which significantly hinder transport along the specified direction. Estimating CPSD and MIP from 3D image data is carried out by using morphological openings [62] and - in case of MIP - the Hoshen-Kopelman algorithm [63]. For a formal definition of constrictivity within the framework of random closed sets, we refer to [54].

3.7. Effective tortuosity

Apart from the purely geometrical characteristics that have been introduced so far in Section 3, we additionally consider effective tortuosity. This quantity is an important microstructure-dependent property of battery electrodes. Effective tortuosity is defined as $\tau^{\mathsf{eff}} = \frac{D\,\varepsilon}{D_{\mathsf{eff}}}$, where D is the intrinsic diffusivity of the phase under consideration (also denoted as "conducting phase") and D_{eff} the effective diffusivity of that phase restricted by a second phase [64]. Note that $\varepsilon \in [0, 1]$ denotes the volume fraction of the "conducting phase", which will be the pore space in our case since due to the high volume fraction of the solid phase in graphite anodes, the limiting factor for battery capacity is frequently the diffusion of lithium ions through the electrolyte [65]. Furthermore, it holds $\tau^{\mathsf{eff}} \geq 1$, see Equation 21.14 in [59]. Effective tortuosity is one of the most influencing characteristics with regard to electrochemical performance of battery electrodes and quantifies the extent to which transport through a porous medium is limited [66, 67]. Therefore, a lot of effort is made to quantitatively access effective tortuosity by impedance spectroscopy [68] or tomographic imaging [69, 70]. With regard to the present paper, it is crucial that the simulated 3D microstructures of the considered graphite anodes adequately reflect the behaviour of effective tortuosity. Since it has been shown in [26] that effective tortuosity can strongly vary locally, we will put a particular focus on the distribution of local effective tortuosity during model fitting, see Section 4.2. Similar to mean geodesic tortuosity, we compute effective tortuosity τ^{eff} in z-direction, where we use the TauFactor application [64].

3.8. Local characteristics

Until now, we only considered "global" characteristics in the sense that we estimate each quantity once using the entire sampling window with a size of $1400 \times 1400 \times 79$ voxels. However, as already pointed out in Section 1, local heterogeneity also significantly influences the performance of lithium-ion batteries. Thus, we compute the empirical distributions of local characteristics by splitting the sampling window into 400 non-overlapping cutouts each with a size of $70 \times 70 \times 79$ voxels. In particular, the distribution of certain quantity q, which arises from computing the quantity q on the above-mentioned 400 cutouts, will be denoted by $\mathbf{q}$. In addition, we will often refer to the mean $\mu(\mathbf{q})$, variance $\sigma^2(\mathbf{q})$ and standard deviation $\sigma(\mathbf{q})$ of the distribution $\mathbf{q}$. Note that, when computing local mean geodesic tortuosity on a cutout, one has to consider only shortest paths starting within the cutout. However, these paths are allowed to leave the cutout since otherwise a systematic bias would be introduced, see [71] for further details.

4. Stochastic 3D microstructure modeling

In this section, we describe two stochastic 3D microstructure models, so-called random set models, which will be used for generating virtual but realistic 3D microstructures of anodes. The models are fitted to tomographic image data by minimizing a cost function that is based on the distribution of local effective tortuosity. Moreover, the fitted models are validated by comparing structural characteristics, which have not been used for model fitting, computed on tomographic image data as well as on model realizations.

4.1. Description of random set models

The starting point in the construction of both random set models are Gaussian random fields [48, 72, 73]. In particular, we will consider standardized Gaussian random fields $\{X(t), t \in \mathbb{R}^3\}$, i.e., we assume that $\mathbb{E}X(t) = 0$ and $\mathrm{Var}X(t) = 1$ for all $t \in \mathbb{R}^3$. Furthermore, we restrict ourselves to stationary and isotropic Gaussian random fields. This directly implies that the distribution of this kind of random fields is uniquely determined by their covariance function $k_X : [0, \infty) \to [-1, 1]$, where the value $k_X(r)$ equals the covariance of $X(t)$ and $X(t+h)$ with $\|h\| = r$.

Stationary and isotropic Gaussian random fields have been used, among others, as versatile tool for modeling the microstructure of three-phase materials. More precisely, pluri-Gaussian models have been applied to gas-diffusion electrodes [74] as well as anodes in solid-oxid fuel cells [75, 76]. With regard to two-phase materials, Gaussian random fields can be used to model the phase of interest by a so-called excursion set $\Xi = \{t \in \mathbb{R}^3 : \ X(t) \geq \lambda\}$ for a fixed, deterministic threshold $\lambda \in \mathbb{R}$. This approach has been successfully applied to solid oxide fuel cell electrodes [77]. However, we remark that it is not directly capable of capturing the 3D microstructure of the graphite anodes considered in the present paper. It turns out that using so-called χ^2-random fields is more suitable for this purpose, see also [78]. Mathematically spoken, a χ^2-random field $\{Y(t), t \in \mathbb{R}^3\}$ with $n \geq 1$ degrees of freedom is given by $Y(t) = \sum_{i=1}^n X_i^2(t)$, where $\{X_1(t)\}, \ldots, \{X_n(t)\}$ are independent standardized Gaussian random fields with one and the same covariance function $k_X : \mathbb{R} \to [-1, 1]$ [48, 72]. Thus, the distribution of a χ^2-random field is uniquely determined by the degree of freedom n and the covariance function k_X of the underlying Gaussian random fields. In the following, we call

$$\Xi_{1,b} = \{t \in \mathbb{R}^3 : Y(t) \geq \lambda_b\} \tag{2}$$

the basic model, where $\lambda_b > 0$ is some threshold. As will be later discussed in Section 4.3, this basic model is able to capture most of the microstructural features of graphite anodes, whereas in particular the goodness of fit with respect to the distribution of local effective tortuosity has to be further improved. It turns out that neither changing the value of n nor the choice of k_X is capable of doing so since the choice of n does not significantly influence the morphology of the corresponding model realizations and k_X can be chosen such that the two-point coverage probability function can be almost perfectly matched, see Sections 4.2.2 and 4.3. This motivates to extend the basic model by modifying the character of the threshold λ_b. More precisely, we consider the extended model

$$\Xi_{1,e} = \{t \in \mathbb{R}^3 : Y(t) \geq \lambda_e + Z(t)\}, \tag{3}$$

where $\{Z(t), t \in \mathbb{R}^3\}$ is a standardized Gaussian random field with a certain covariance function k_Z, which is independent of the random fields $\{X_1(t)\}, \ldots, \{X_n(t)\}$. Note that the quantity $\lambda_e \in \mathbb{R}$ in Eq. (3) will play the same role as $\lambda_b \in \mathbb{R}$ in the basic model, i.e., to ensure that the volume fraction of $\Xi_{1,e}$ matches the volume fraction of the solid phase observed in tomographic image data. By considering a spatially varying random threshold $\{\Lambda(t), t \in \mathbb{R}^3\}$ given by $\Lambda(t) = \lambda_e + Z(t)$ for all $t \in \mathbb{R}^3$ instead of a global deterministic threshold, the distribution of local effective tortuosity can be matched better which will be shown in Section 4.3. The calibration of both, the basic and the extended models to tomographic image data, is described in Section 4.2.

4.2. Model calibration

The calibration of the basic and extended χ^2-models to tomographic image data is a multi-step procedure. To begin with, we start with the basic model, which has the four parameters n, λ_b, a and b, where a and b are given in Eq. (4) below. It turned out that the specific choice of n, i.e. the number of Gaussian random fields considered in the definition of $\{Y(t)\}$, has little influence on the goodness of fit. Therefore, to minimize the computational complexity, we put $n = 2$. Thus, the first step of the fitting procedure concerns the choice of the fixed threshold λ_b considered in Eq. (2). The second step involves the two-point coverage probability function introduced in Eq. (1), where the phase of interest is the solid phase consisting of active material, binder and conductive additives.

4.2.1. Calibration of the basic model

The threshold $\lambda_b > 0$ is chosen such that $\mathbb{P}(Y(0) \geq \lambda_b) = \mathbb{E}\nu_3(\Xi_{1,b} \cap [0,1]^3) = \varepsilon_1$. Because the random variable $Y(0)$ follows a χ^2-distribution with two degrees of freedom, this can be easily achieved by putting λ_b equal to the ε_0-quantile of the χ^2-distribution with two degrees of freedom, which is computed using the Matlab "chi2inv" function. In order to compute the covariance function k_X, we first estimate the two-point coverage probability function $C_{1,1}(r)$ of the solid phase for each distance $r \in \{0, ..., 30\}$, where at a distance of at most 30 voxels (corresponding to 19.62 µm) the value of $C_{1,1}$ approaches ε_1^2 for all six samples. Next, by means of Monte Carlo estimation, we estimate the probability $\mathbb{P}(X_{1,0}^2 + X_{2,0}^2 \geq \lambda_b, X_{1,r}^2 + X_{2,r}^2 \geq \lambda_b)$ using $\ell = 10^6$ realizations, where $(X_{1,0}, X_{1,r})$ and $(X_{2,0}, X_{2,r})$ are two stochastically independent random vectors that follow a two-dimensional standardized Gaussian distribution with $\mathrm{Cov}(X_{1,0}, X_{1,r}) = \mathrm{Cov}(X_{2,0}, X_{2,r}) = \rho$ for some $\rho \geq 0$ [79]. Let $p(\rho)$ denote the above mentioned Monte Carlo estimate of $\mathbb{P}(X_{1,0}^2 + X_{2,0}^2 \geq \lambda_b, X_{1,r}^2 + X_{2,r}^2 \geq \lambda_b)$, which should be equal to $C_{1,1}(r)$ in order to ensure that the two-point coverage probability function computed from tomographic image data is matched. Thus, for each distance r_i with $r_i \in \{0, ..., 30\}$ the value of ρ_i is chosen such that we minimize the cost function $\zeta(\rho_i) = |p(\rho_i) - C_{1,1}(r_i)|$ using the "fminbnd" command in Matlab, see [80, 81]. Note that we assume that $k_X(r) \geq 0$ for all $r \geq 0$. In order to obtain a parametric representation of $\rho_0, ..., \rho_{30}$, the covariance function k_X is then fitted with a Cauchy template function, i.e., we assume that

$$k_X(r) = (1 + (ar)^2)^{-b} \tag{4}$$

for some parameters $a, b > 0$, which are determined by the least-squares method implemented in Matlab [82, 83, 84]. This type of covariance function as well as further frequently used parametric families of covariance functions can be found e.g. in [48, 85]. At this point, the fitting of the basic model is complete. In order to simulate the excursion set $\Xi_{1,b}$ of the calibrated basic model, the simulation of the Gaussian random fields $\{X_1(t)\}$ and $\{X_2(t)\}$ is carried out using the algorithm described in [86].

Note that various global morphological properties of simulated 3D microstructures drawn from the calibrated basic model are comparable to corresponding properties of tomographic image data, see

Section 4.3 for details. However, important local morphological properties do diverge significantly, which motivates the replacement of the basic model $\Xi_{1,b}$ by the extended model $\Xi_{1,e}$ given in Eq. (3), considering a spatially varying random threshold.

4.2.2. Calibration of the extended model

The fitting procedure for the extended model is similar compared to that of the basic model. First, the parameter $\lambda_e > 0$ is chosen such that $\mathbb{P}(Y(0) + Z(0) \geq \lambda_e) = \mathbb{E}\nu_3(\Xi_{1,e} \cap [0,1]^3) = \varepsilon_1$. This can be achieved by setting λ_e equal to the ε_0-quantile of the distribution of $Y(0) + Z(0)$, where $Y(0)$ follows a χ^2-distribution with $n = 2$ degrees of freedom and $Z(0)$ is a random variable with standard normal distribution that is stochastically independent of $Y(0)$. In order to estimate this quantile, we use a Monte Carlo approach and draw 10^6 realizations from $Y(0)$ and $Z(0)$, respectively. This allows us to estimate the empirical cumulative distribution function of $Y(0) + Z(0)$ from which the above mentioned quantile can be computed.

Furthermore, the fitting of the covariance function k_X is done in exactly the same way as it is described for the basic model, see Section 4.2.1. Note that this step assumes that the additional introduction of a spatially varying field $\{Z(t)\}$ does not affect the fitting of k_X, which will be discussed later on, based on the plot on the left-hand side of Figure 2 in Section 4.3. In addition, we now have to choose the covariance function k_Z of the spatially-varying level-set field $\{\Lambda(t)\}$ in a meaningful way. As covariance function for this field, the following parametric family given by $k_Z(r) = \exp(-c \cdot r)$ with $c > 0$ as fitting parameter was chosen to keep the number of model parameters and thus the complexity of the model low.
In order to determine the value of c, we define a cost function based on the distribution of local effective tortuosity of the pore phase. More precisely, the cost function $\zeta : (0, \infty) \to [0, \infty)$ is given by

$$\zeta(c) = \frac{|\mu(\boldsymbol{\tau}^{\mathbf{eff}}_{\mathbf{0},\boldsymbol{d}}) - \mu(\boldsymbol{\tau}^{\mathbf{eff}}_{\mathbf{0},\boldsymbol{e}})|}{\mu(\boldsymbol{\tau}^{\mathbf{eff}}_{\mathbf{0},\boldsymbol{d}})} + \frac{|\sigma^2(\boldsymbol{\tau}^{\mathbf{eff}}_{\mathbf{0},\boldsymbol{d}}) - \sigma^2(\boldsymbol{\tau}^{\mathbf{eff}}_{\mathbf{0},\boldsymbol{e}})|}{\sigma^2(\boldsymbol{\tau}^{\mathbf{eff}}_{\mathbf{0},\boldsymbol{d}})}. \tag{5}$$

The index k of $\boldsymbol{\tau}^{\mathbf{eff}}_{\mathbf{0},\boldsymbol{k}}$ corresponds to tomographic image data ($k = d$) and the extended model ($k = e$), respectively. In order to keep the computational complexity low, we used one model realization for estimating $\mu(\boldsymbol{\tau}^{\mathbf{eff}}_{\mathbf{0},\boldsymbol{e}})$ and $\sigma^2(\boldsymbol{\tau}^{\mathbf{eff}}_{\mathbf{0},\boldsymbol{e}})$, respectively. The numerical optimization using the cost function given in Equation (5) has been carried out by the Matlab surrogate optimizer [87]. Thus, the parameters a and b allow us to match a geometrical descriptor of 3D microstructure, namely the two-point coverage probability function, whereas the introduction of the parameter c in the extended model allows us to significantly improve the goodness of fit with regard to a functional characteristic, namely effective tortuosity, at the same time.

Furthermore, a final smoothing step has been applied to the realizations of the extended model in order to obtain even more realistic microstructures. This post-processing step, among others, reduces isolated voxels of the solid phase. For this purpose, a Gaussian filter with $\sigma_x = \sigma_y = \sigma_z = 1$ [46, 88] and subsequent global thresholding has been used, where the global threshold has been chosen in such a way that the volume fraction of the solid phase is matched. Note that this kind of smoothing is frequently used in the literature [32, 75, 89].

	A_1	A_2	B_1	B_2	C_1	C_2
λ_b	0.95	0.68	0.77	0.52	0.89	0.57
a	0.0036	0.0038	0.0048	0.0041	0.1295	0.1751
b	1598.29	1135.09	1083.2	1141.24	1.11	0.74
λ_e	1.05	0.67	0.81	0.4	0.98	0.49
c	0.41	0.31	0.34	0.38	0.22	0.5

Table 1: Model parameters of the calibrated random set models for each of the six samples. Note that the value of c is only used in the extended model, whereas the parameters a and b are used in the basic as well as the extended model.

The resulting model parameters a, b, c and λ_b, λ_e of the calibrated random set models are listed in Table 1. In addition, a first visual impression of the goodness of fit is shown in Figure 1, where two-dimensional cutouts of simulated microstructures created with the basic and extended model are shown together with their tomographic counterparts. A formal model validation is carried out in Section 4.3.

4.3. Model validation

In this section, the basic model and the extended model are validated by comparing several microstructure characteristics of tomographic and simulated image data. Thus, tomographic image data is used as ground truth in order to quantify the goodness of fit of both 3D microstructure models. Note that all direction-dependent characteristics have been computed with regard to the z-direction, which corresponds to the main direction of electrical and ionic transport. This direction is also known as through-plane direction. All results shown in this section are averaged over ten model realizations, where the size of the sampling window equals the size of tomographic image data. For the sake of clarity, model validation is described in detail with regard to the samples A1 and A2, whereas the results of the model validation with regard to the other four samples are just shown in Table 2. At first, we discuss the two point coverage probability function $C_{1,1}$ as well as the distribution of local effective tortuosity, which have been used for model fitting.

4.3.1. Characteristics used for model fitting

As shown in Figure 2, the centered two-point coverage probability function (i.e. $C_{1,1} - \varepsilon_1^2)$) is nicely matched by both random set models. In particular, the introduction of the spatially-varying threshold field $\{\lambda_e + Z(t)\}$ together with the final smoothing step does not change the two-point coverage probability function significantly. Thus, it is reasonable to compute the covariance function k_X for the fitting of the extended model in the same way as for the calibration of the basic model. On the other hand, the distributions of local effective tortuosity are considerably closer to the one of the tomographic data when considering the extended model compared to the basic model, both, with regard to samples A1 and A2, see Figure 2. This significant improvement is of central importance with regard to the simulation of electrochemical properties as already discussed in Section 3.7. As it can be seen in Table 2, similar results are obtained with regard to the other samples as well.

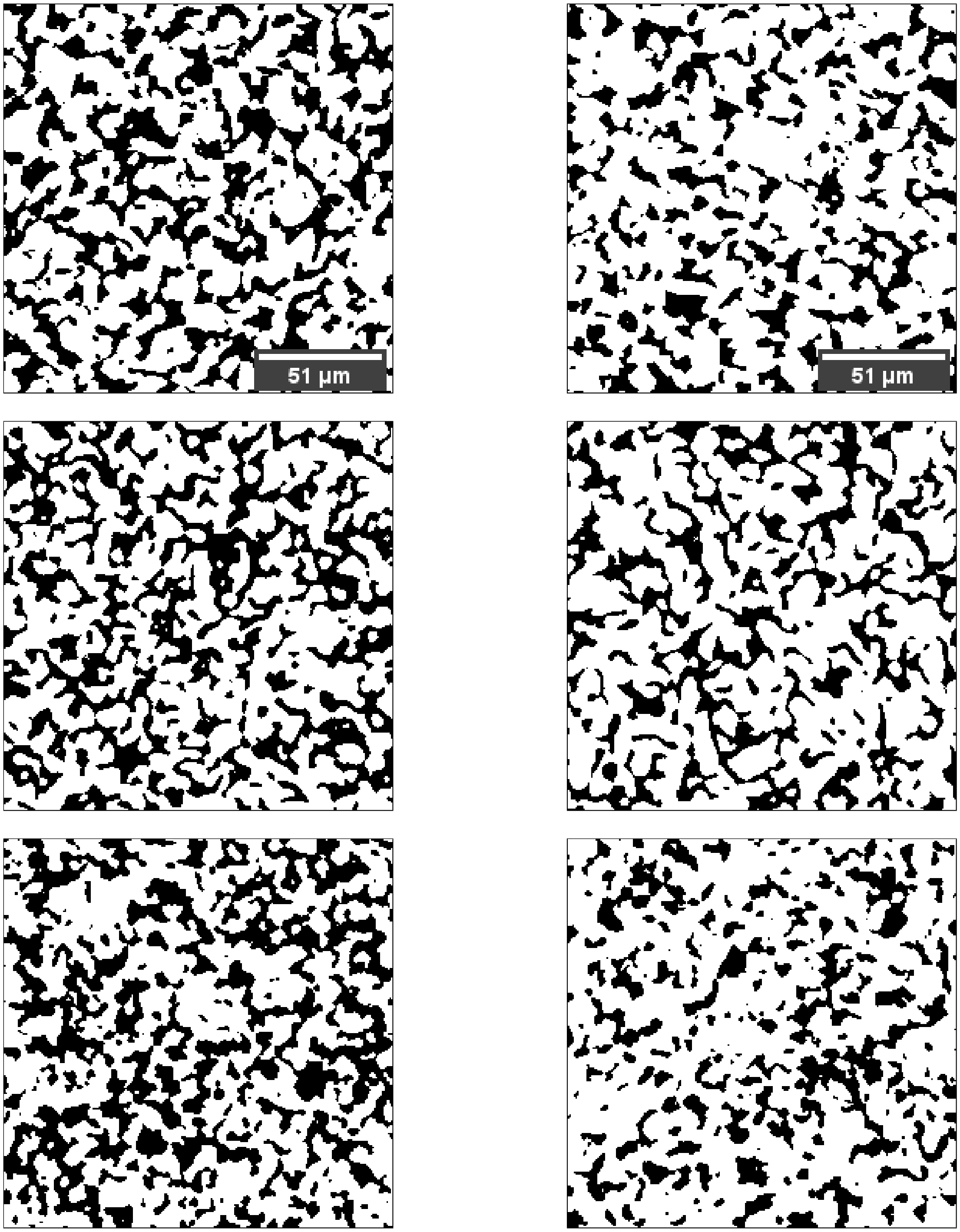

Figure 1: Two-dimensional cutouts (160.5 µm × 160.5 µm) of tomographic image data (top) and simulated microstructures created by the basic model (middle) and extended model (bottom). The solid phase consisting of active material, binder and conductive additives is depicted in white, whereas the black phase corresponds to the pore space. The respective structures of sample A1 and sample A2 are shown in the left and right column, respectively.

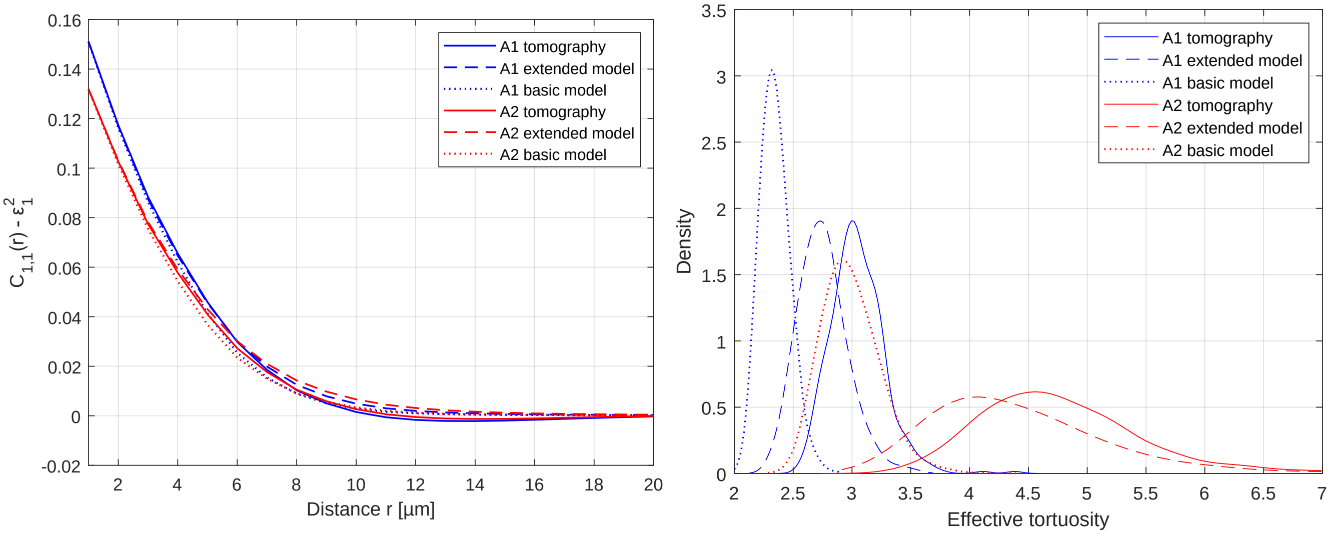

Figure 2: Centered two-point coverage probability function $C_{1,1}$ (left) and distribution of local effective tortuosity (right) of samples A1 (blue curves) and A2 (red curves). The results for tomographic image data and the extended as well as the basic model are represented by the solid, dashed and dotted lines, respectively.

4.3.2. Characteristics not used for model fitting

Next, model validation is carried out with regard to microstructure characteristics that have not been used for model fitting. At first, geodesic tortuosity is discussed, which allows us to quantify the length of shortest transportation paths. As can be seen in Figure 3, the improvement with respect to this characteristic is comparable to the one achieved with regard to effective tortuosity when considering the pore phase, i.e., the peaks are closer together and the widths of the distributions are more similar. This does not only hold for samples A1 and A2, see Table 2. With regard to shortest paths within the solid phase, the basic model seems to match this quantity better. However, the scale of the x-axis in the plot on the right-hand side of Figure 3 indicates that due to the large volume fraction of the solid phase, the values of geodesic tortuosity are close to one such that the relative error of the extended model is rather small.

In addition to the previously discussed global geodesic tortuosity, we now consider the distribution of local mean geodesic tortuosity, which emerges by computing mean geodesic tortuosity on each each of the 400 non-overlapping cutouts described in Section 3.8. Figure 4 shows a similar pattern compared to the plot on the left-hand side of Figure 3, i.e., the extended model is preferable in comparison to the basic model since the location and the shape of the distribution of local mean geodesic tortuosity is then much closer to the distribution corresponding to tomographic image data.

Next, we consider the distribution of local volume fraction of the solid phase, see the plot on the left-hand side of Figure 5. Since the fixed threshold λ_b as well as the threshold λ_e corresponding to the extended model are chosen such that the volume fraction of the solid phase ε_1 matches on average the volume fraction observed in tomographic image data, it is no surprise that $\mu(\boldsymbol{\varepsilon_1})$, which equals the overall volume fraction ε_1, is matched by both random set models. As can be seen in Table 2, this statement is also true with regard to the other samples. In addition, both models are capable of matching the standard deviation $\sigma(\boldsymbol{\varepsilon_1})$, too. Table 2 shows that the extended model

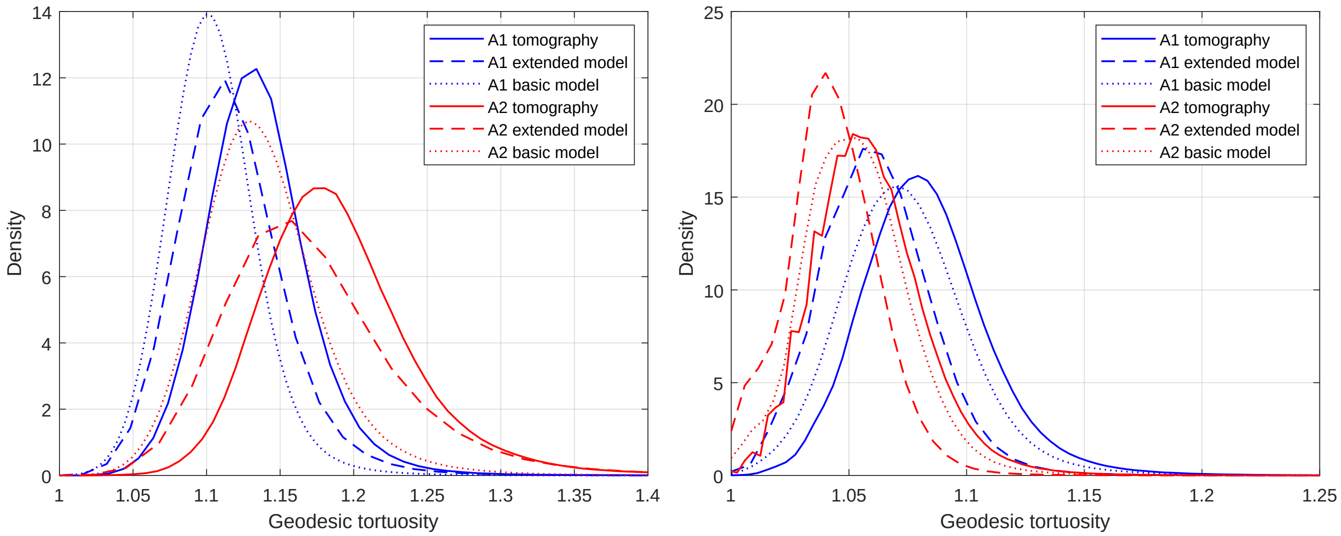

Figure 3: Distribution of geodesic tortuosity of the pore space (left) and the solid phase (right) of samples A1 (blue curves) and A2 (red curves). The tomographic data and the extended as well as the basic model are represented by the solid, dashed and dotted lines, respectively.

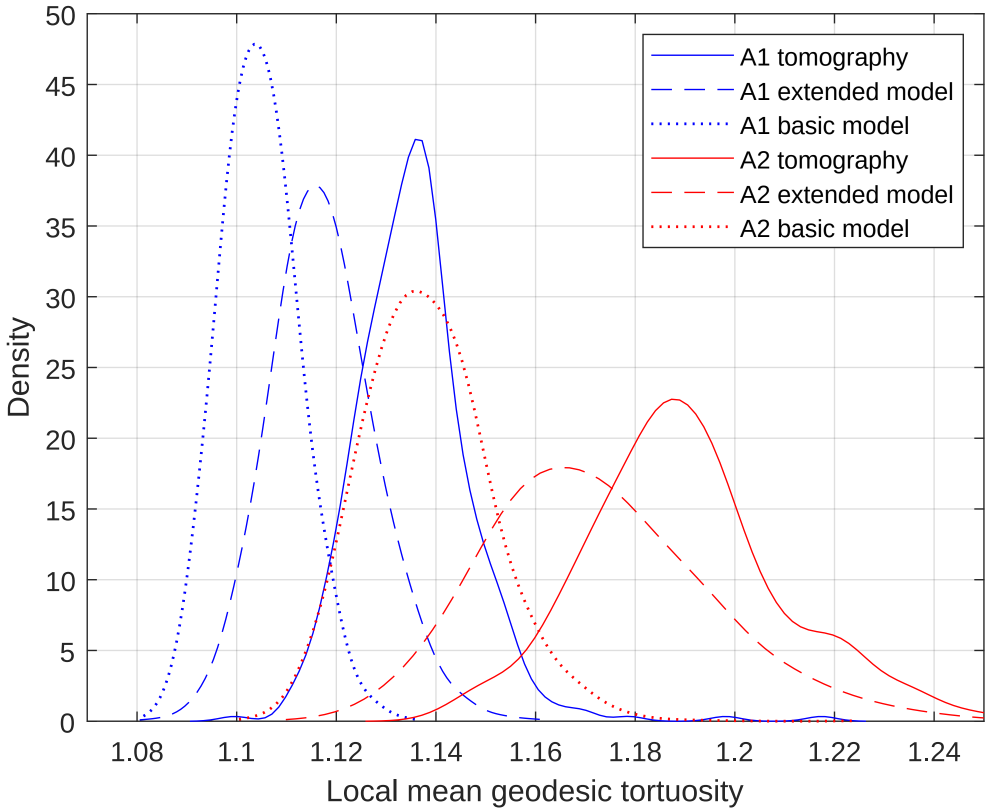

Figure 4: Distribution of local mean geodesic tortuosity of samples A1 (blue curves) and A2 (red curves). The results for tomographic image data and the extended as well as the basic model are represented by the solid, dashed and dotted lines, respectively.

improves the goodness of fit with respect to $\sigma(\boldsymbol{\varepsilon_1})$ in four of six cases. With regard to samples A1 and C1, the basic model leads to slightly better results.

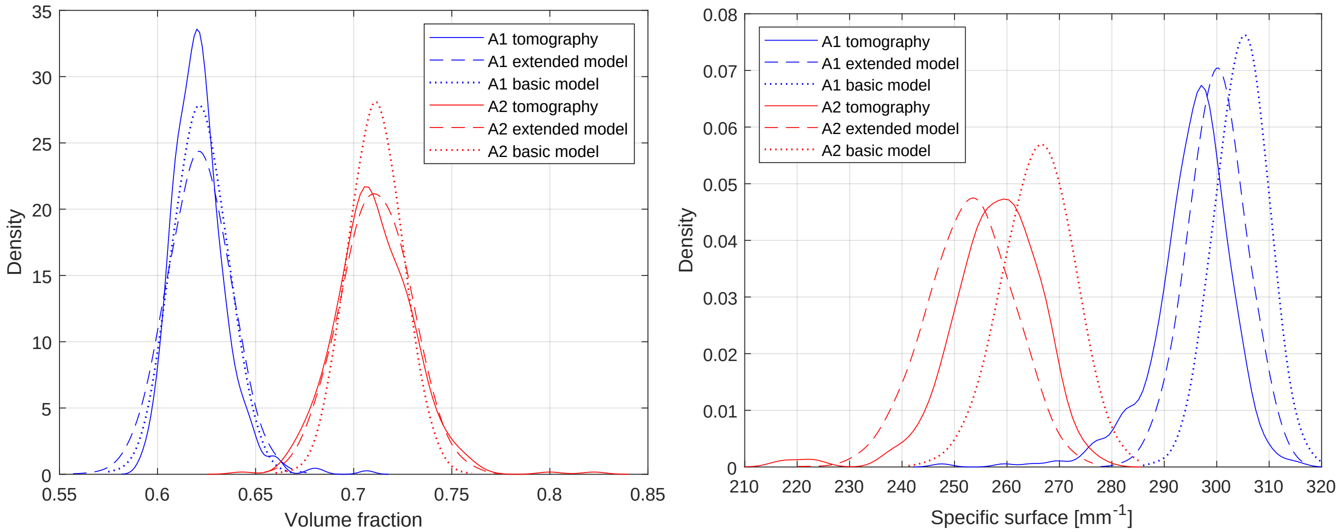

Figure 5: Distribution of local volume fraction of the solid phase consisting of active material, binder and conductive additives (left) and local specific surface area (right) of samples A1 (blue curves) and A2 (red curves). The results for tomographic image data and the extended as well as the basic model are represented by the solid, dashed and dotted lines, respectively.

Next, model validation is carried out with respect to the distribution of local specific surface area, see the plot on the right-hand side of Figure 5. With regard to sample A1, both random set models slightly overestimate the mean value of this distribution. In case of sample A2, both models lead to almost the same goodness of fit.

With regard to continuous phase size distribution of the pore phase, the extended model again seems to match the tomographic data better than the basic model, see the plot on the left-hand side of Figure 6. In particular, the extended model leads to a significant improvement compared to the model with a fixed threshold λ_b when considering sample A2. Furthermore, the plot on the right-hand side of Figure 6 shows that both random set models lead to a good accordance between simulated 3D microstructures and tomographic image data with regard to the continuous phase distribution computed on the solid phase.

The plots corresponding to MIP of the pore phase show the same pattern compared to the continuous pore size distribution, which can be seen in the plot on the left-hand side of Figure 7. When considering the solid phase, there is a slight disagreement in the range between 2 and 3 µm (sample A1) and between 3 and 4 µm (sample A2), respectively.

Based on the continuous phase size distribution and the results of simulated mercury intrusion, constrictivity is computed for both phases. As shown in Table 2, the extended model leads to lower or approximately equal mean absolute percentage errors compared to the basic model, where B1 is the only sample, for which the random set model with a fixed threshold leads to a noticeable

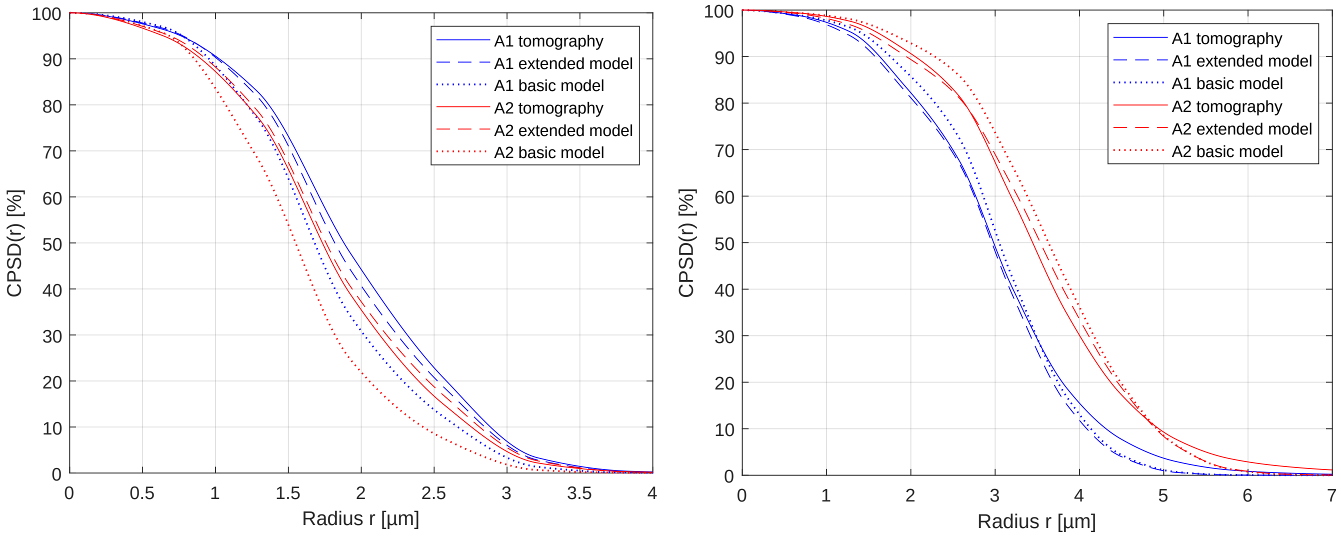

Figure 6: Continuous phase size distribution of the pore phase (left) and the solid phase (right) of samples A1 (blue curves) and A2 (red curves). The results for tomographic image data and the extended as well as the basic model are represented by the solid, dashed and dotted lines, respectively.

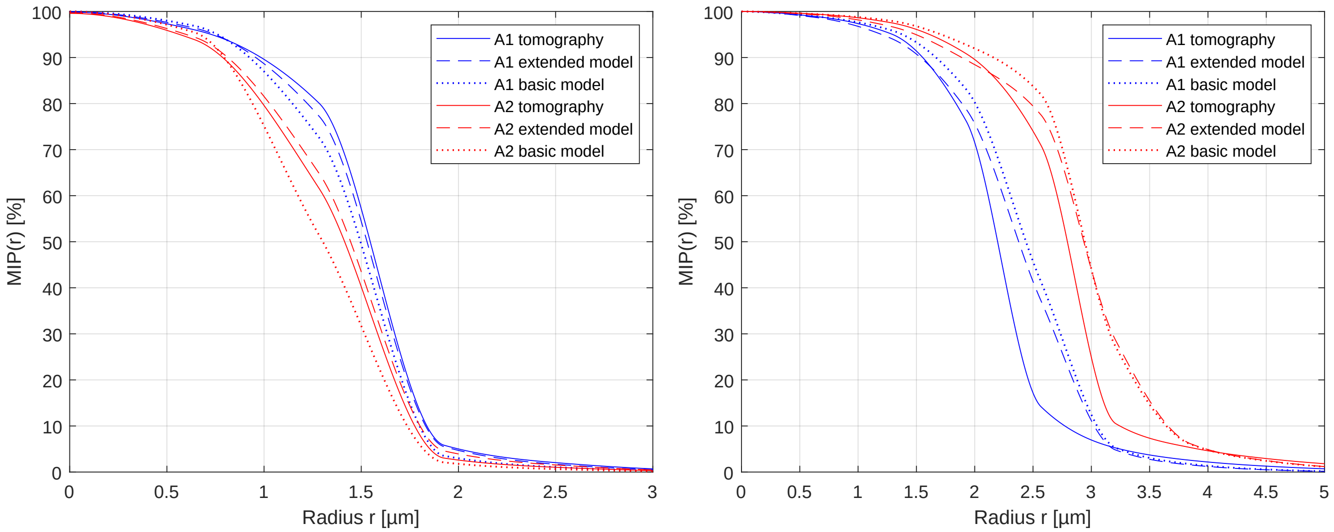

Figure 7: Simulated mercury intrusion porosimetry of the pore phase (left) and the solid phase (right) of samples A1 (blue curves) and A2 (red curves). The results for tomographic image data and the extended as well as the basic model are represented by the solid, dashed and dotted lines, respectively.

better fit with regard to constrictivity.

As can be seen in Figure 8, the distribution of chord lengths of both phases of samples A1 and A2 is matched by both models equally well, where minor differences can be detected for short chord lengths. With regard to the other samples, one can observe a general improvement when using the extended model compared to the basic model, see Table 2.

Hence, it can be concluded that using a spatially varying threshold field $\{\Lambda(t)\}$ instead of a global

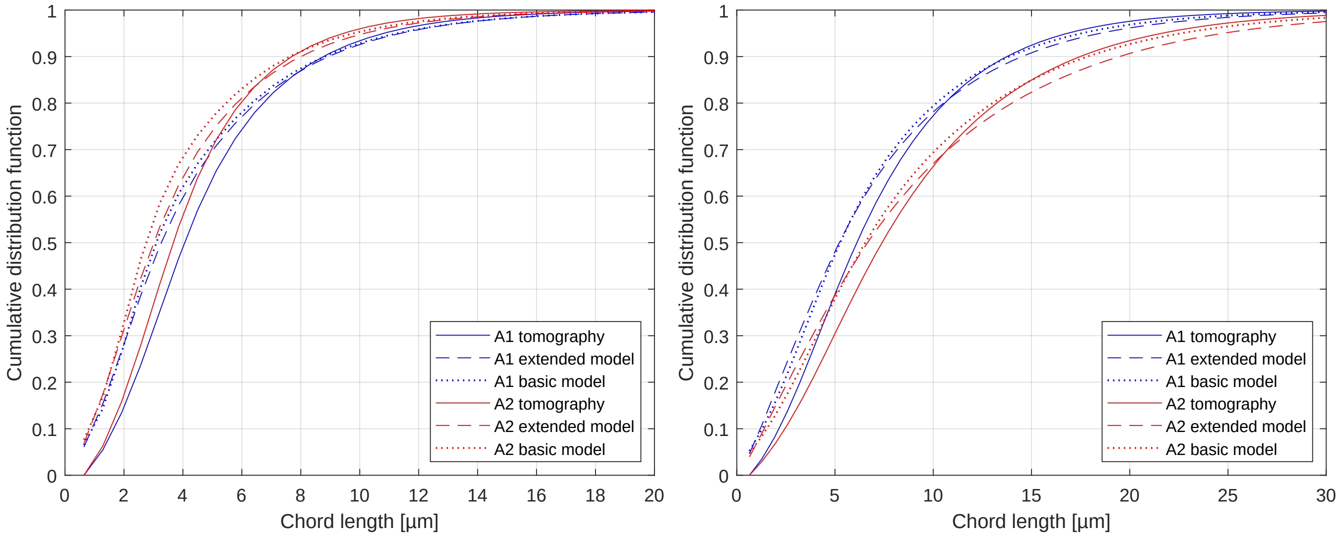

Figure 8: Chord length distribution of the pore phase (left) and the solid phase (right) of samples A1 (blue curves) and A2 (red curves). The results for tomographic image data and the extended as well as the basic model are represented by the solid, dashed and dotted lines, respectively.

threshold λ_b improves the goodness of fit with regard to most characteristics under consideration. In particular, the dramatic improvement with regard to the local distribution of effective tortuosity by the introduction of an additional model parameter corresponding to the spatially varying threshold field is of great importance when using simulated 3D microstructures as structural input for spatially resolved numerical simulations of electrochemical properties.

5. Conclusion and outlook

In this paper, we considered two random set models based on χ^2-random fields for modelling the 3D microstructure of six differently manufactured graphite anodes, where 3D image data has been obtained by synchrotron tomography. The basic model describes the solid phase by an excursion set of a χ^2-random field using a fixed threshold, whereas the extended model is based on a spatially varying threshold. Both models have been validated by comparing microstructure-dependent characteristics of tomographic and simulated image data, where a particular focus has been put on effective tortuosity and local heterogeneity, which has been quantified by computing the quantities computed for 400 small cutouts. It has been shown that the extended model outperforms the basic model and is able to generate realistic 3D morphologies of graphite anodes. Thus, the presented stochastic 3D microstructure model based on a spatially varying threshold can be used in the future to generate a wide spectrum of virtual but realistic morphologies by systematic variation of the model parameters. Due to significantly improved fit of the extended model with regard to the local distribution of effective tortuosity compared to the basic model, these structures can then be used for spatially resolved numerical simulations of electrochemical performance to establish microstructure-property relationships as well as to generate structuring recommendations for the design of graphite anodes with optimized electrochemical properties.

Descriptor	A1	A2	B1	B2	C1	C2
$\mu(\boldsymbol{\tau}^{\mathbf{eff}}_{\mathbf{0},\boldsymbol{e}})$	2.75 (10)	4.42 (8)	3.7 (6)	7.7 (2)	3.24 (10)	6.95 (9)
$\mu(\boldsymbol{\tau}^{\mathbf{eff}}_{\mathbf{0},\boldsymbol{b}})$	2.35 (23)	2.99 (38)	2.78 (29)	3.8 (52)	2.74 (24)	4.71 (38)
$\sigma(\boldsymbol{\tau}^{\mathbf{eff}}_{\mathbf{0},\boldsymbol{e}})$	0.21 (6)	0.78 (4)	0.42 (4)	2.3 (12)	0.64 (10)	2.78 (6)
$\sigma(\boldsymbol{\tau}^{\mathbf{eff}}_{\mathbf{0},\boldsymbol{b}})$	0.13 (43)	0.25 (67)	0.15 (65)	0.35 (83)	0.33 (43)	1.53 (48)
$\mathrm{Cl}_{0,e}$ [µm]	4.6 (10)	4.19 (9)	4.01 (13)	3.51 (17)	5.09 (4)	3.48 (17)
$\mathrm{Cl}_{0,b}$ [µm]	4.51 (12)	3.97 (13)	3.6 (22)	3.2 (24)	4.58 (14)	3.15 (25)
$\mathrm{Cl}_{1,e}$ [µm]	7.13 (6)	9.21 (1)	7.81 (7)	10.15 (7)	8.35 (0)	9.23 (9)
$\mathrm{Cl}_{1,b}$ [µm]	7 (7)	8.77 (5)	7.07 (15)	9.36 (15)	7.58 (9)	8.48 (16)
A_e $[\mathrm{mm}]^{-1}$	300 (2)	253 (2)	295 (5)	243 (2)	255 (5)	265 (6)
A_b $[\mathrm{mm}]^{-1}$	305 (3)	266 (3)	330 (7)	267 (8)	285 (6)	291 (16)
$\tau^{\mathrm{geo}}_{0,e}$	1.117 (2)	1.172 (2)	1.149 (1)	1.238 (0)	1.13 (3)	1.214 (2)
$\tau^{\mathrm{geo}}_{0,b}$	1.104 (3)	1.138 (4)	1.125 (3)	1.169 (6)	1.118 (4)	1.177 (5)
$\tau^{\mathrm{geo}}_{1,e}$	1.06 (2)	1.041 (2)	1.047 (0)	1.031 (0)	1.055 (2)	1.034 (1)
$\tau^{\mathrm{geo}}_{1,b}$	1.074 (1)	1.053 (1)	1.06 (1)	1.041 (1)	1.066 (1)	1.042 (0)
$\beta_{0,e}$	0.71 (5)	0.68 (1)	0.7 (21)	0.41 (3)	0.56 (2)	0.42 (2)
$\beta_{0,b}$	0.79 (17)	0.71 (6)	0.53 (8)	0.59 (49)	0.76 (32)	0.56 (34)
$\beta_{1,e}$	0.64 (19)	0.69 (5)	0.73 (19)	0.71 (1)	0.71 (12)	0.74 (7)
$\beta_{1,b}$	0.64 (18)	0.66 (0)	0.62 (2)	0.67 (3)	0.71 (13)	0.73 (6)
$\mu(\boldsymbol{\tau}^{\mathrm{geo}}_{\mathbf{0},\boldsymbol{e}})$	1.117 (2)	1.172 (1)	1.149 (1)	1.239 (0)	1.131 (2)	1.216 (2)
$\mu(\boldsymbol{\tau}^{\mathrm{geo}}_{\mathbf{0},\boldsymbol{b}})$	1.105 (3)	1.138 (4)	1.125 (3)	1.17 (6)	1.119 (3)	1.178 (5)
$\sigma(\boldsymbol{\tau}^{\mathrm{geo}}_{\mathbf{0},\boldsymbol{e}})$	0.011 (10)	0.022 (9)	0.015 (5)	0.034 (4)	0.02 (13)	0.033 (19)
$\sigma(\boldsymbol{\tau}^{\mathrm{geo}}_{\mathbf{0},\boldsymbol{b}})$	0.008 (33)	0.013 (39)	0.008 (41)	0.015 (58)	0.014 (40)	0.025 (39)
$\mu(\boldsymbol{\varepsilon}_{\mathbf{1},\boldsymbol{e}})$	0.621 (0)	0.711 (0)	0.679 (0)	0.771 (0)	0.639 (0)	0.752 (0)
$\mu(\boldsymbol{\varepsilon}_{\mathbf{1},\boldsymbol{b}})$	0.622 (0)	0.711 (0)	0.68 (0)	0.77 (0)	0.639 (0)	0.752 (0)
$\sigma(\boldsymbol{\varepsilon}_{\mathbf{1},\boldsymbol{e}})$	0.016 (16)	0.018 (12)	0.015 (2)	0.013 (20)	0.029 (26)	0.022 (16)
$\sigma(\boldsymbol{\varepsilon}_{\mathbf{1},\boldsymbol{b}})$	0.014 (0)	0.014 (32)	0.011 (30)	0.011 (37)	0.023 (1)	0.021 (19)
$\mu(\boldsymbol{A_e})$ $[\mathrm{mm}]^{-1}$	300 (2)	253 (2)	295 (5)	243 (2)	255 (5)	265 (6)
$\mu(\boldsymbol{A_b})$ $[\mathrm{mm}]^{-1}$	305 (3)	266 (3)	330 (7)	267 (8)	285 (6)	291 (16)
$\sigma(\boldsymbol{A_e})$ $[\mathrm{mm}]^{-1}$	5.58 (27)	8.08 (17)	6.65 (14)	8.62 (13)	10.52 (23)	17.7 (0)
$\sigma(\boldsymbol{A_b})$ $[\mathrm{mm}]^{-1}$	5 (35)	6.7 (31)	5.49 (5)	7.25 (27)	11.19 (18)	19.73 (11)

Table 2: Distributional descriptors of all considered image characteristics. The values within parenthesis denote the mean absolute percentage error (MAPE) in % with respect to tomographic image data, i.e., tomographic image data is used as ground truth for computing the errors.

Data availability

The raw/processed data required to reproduce these findings cannot be shared at this time as the data also forms part of an ongoing study.

References

[1] R. Korthauer, Lithium-Ion Batteries: Basics and Applications. Berlin: Springer, 2018.

[2] B. Scrosati, K. M. Abraham, W. van Schalkwijk, and J. Hassoun, eds., Lithium Batteries: Advanced Technologies and Applications. The Electrochemical Society Series, Hoboken: J. Wiley & Sons, 2013.

[3] J. B. Goodenough and K.-S. Park, "The Li-ion rechargeable battery: A perspective," Journal of the American Chemical Society, vol. 135, no. 4, p. 1167–1176, 2013.

[4] J. Meng, Y. Suo, J. Li, G. Zheng, Y. Liu, J. Zhang, and X. Zheng, "Nitrogen-doped graphene aerogels as anode materials for lithium-ion battery: Assembly and electrochemical properties," Materials Letters, vol. 160, p. 392–396, 2015.

[5] Q. Lian, G. Zhou, X. Zeng, C. Wu, Y. Wei, C. Cui, W. Wei, L. Chen, and C. Li, "Carbon coated SnS/SnO_2 heterostructures wrapping on CNFs as an improved-performance anode for Li-ion batteries: Lithiation-induced structural optimization upon cycling," ACS Applied Materials & Interfaces, vol. 8, no. 44, p. 30256–30263, 2016.

[6] J. Wang, N. Yang, H. Tang, Z. Dong, Q. Jin, M. Yang, D. Kisailus, H. Zhao, Z. Tang, and D. Wang, "Accurate control of multishelled Co_3O_4 hollow microspheres as high-performance anode materials in lithium-ion batteries," Angewandte Chemie International Edition, vol. 52, no. 25, p. 6417–6420, 2013.

[7] Y. Xing, Y.-B. He, B. Li, X. Chu, H. Chen, J. Ma, H. Du, and F. Kang, "$LiFePO_4$/C composite with 3D carbon conductive network for rechargeable lithium ion batteries," Electrochimica Acta, vol. 109, p. 512–518, 2013.

[8] A. Vu, Y. Qian, and A. Stein, "Porous electrode materials for lithium-ion batteries – how to prepare them and what makes them special," Advanced Energy Materials, vol. 2, no. 9, p. 1056–1085, 2012.

[9] B. Wang, T. Liu, A. Liu, G. Liu, L. Wang, T. Gao, D. Wang, and X. S. Zhao, "A hierarchical porous C@$LiFePo_4$/carbon nanotubes microsphere composite for high-rate lithium-ion batteries: Combined experimental and theoretical study," Advanced Energy Materials, vol. 6, no. 16, p. 1600426, 2016.

[10] S. Cho, C.-F. Chen, and P. P. Mukherjee, "Influence of microstructure on impedance response in intercalation electrodes," Journal of The Electrochemical Society, vol. 162, no. 7, p. A1202–A1214, 2015.

[11] X. Huang, J. Tu, X. Xia, X. Wang, J. Xiang, L. Zhang, and Y. Zhou, "Morphology effect on the electrochemical performance of NiO films as anodes for lithium ion batteries," Journal of Power Sources, vol. 188, no. 2, p. 588–591, 2009.

[12] G. Lenze, H. Bockholt, C. Schilcher, L. Froböse, D. Jansen, U. Krewer, and A. Kwade, "Impacts of variations in manufacturing parameters on performance of lithium-ion batteries," Journal of The Electrochemical Society, vol. 165, no. 2, p. A314–A322, 2018.

[13] W. Li and J. C. Currie, “Morphology effects on the electrochemical performance of $\mathrm{LiNi}_{1-x}\mathrm{Co}_x\mathrm{O}_2$,” Journal of The Electrochemical Society, vol. 144, no. 8, p. 2773–2779, 1997.

[14] Y. Shin and A. Manthiram, “Influence of microstructure on the electrochemical performance of $\mathrm{LiMn}_{2-y-z}\mathrm{Li}_y\mathrm{Ni}_z\mathrm{O}_4$ spinel cathodes in rechargeable lithium batteries,” Journal of Power Sources, vol. 126, no. 1, p. 169–174, 2004.

[15] A. H. Wiedemann, G. M. Goldin, S. A. Barnett, H. Zhu, and R. J. Kee, “Effects of three-dimensional cathode microstructure on the performance of lithium-ion battery cathodes,” Electrochemica Acta, vol. 88, p. 580–588, 2013.

[16] H. Bockholt, M. Indrikova, A. Netz, F. Golks, and A. Kwade, “The interaction of consecutive process steps in the manufacturing of lithium-ion battery electrodes with regard to structural and electrochemical properties,” Journal of Power Sources, vol. 325, p. 140–151, 2016.

[17] L. S. Kremer, A. Hoffmann, T. Danner, S. Hein, B. Prifling, D. Westhoff, C. Dreer, A. Latz, V. Schmidt, and M. Wohlfahrt-Mehrens, “Manufacturing process for improved ultra-thick cathodes in high-energy lithium-ion batteries,” Energy Technology, vol. 8, no. 2, p. 1900167, 2020.

[18] H. Bockholt, W. Haselrieder, and A. Kwade, “Intensive dry and wet mixing influencing the structural and electrochemical properties of secondary lithium-ion battery cathodes,” ECS Transactions, vol. 50, p. 25–35, 2013.

[19] H. Zheng, L. Tan, G. Liu, X. Song, and V. S. Battaglia, “Calendering effects on the physical and electrochemical properties of $\mathrm{Li[Ni}_{1/3}\mathrm{Mn}_{1/3}\mathrm{Co}_{1/3}]\mathrm{O}_2$ cathode,” Journal of Power Sources, vol. 208, p. 52–57, 2012.

[20] W. Haselrieder, S. Ivanov, D. K. Christen, H. Bockholt, and A. Kwade, “Impact of the calendering process on the interfacial structure and the related electrochemical performance of secondary lithium-ion batteries,” ESC Transactions, vol. 50, no. 26, p. 59–70, 2013.

[21] K. Kuchler, B. Prifling, D. Schmidt, H. Markötter, I. Manke, T. Bernthaler, V. Knoblauch, and V. Schmidt, “Analysis of the 3D microstructure of experimental cathode films for lithium-ion batteries under increasing compaction,” Journal of Microscopy, vol. 272, no. 2, p. 96–110, 2018.

[22] A. Latz and J. Zausch, “Multiscale modeling of lithium ion batteries: thermal aspects,” Beilstein Journal of Nanotechnology, vol. 6, no. 1, p. 987–1007, 2015.

[23] W. A. Paxton, Z. Zhong, and T. Tsakalakos, “Tracking inhomogeneity in high-capacity lithium iron phosphate batteries,” Journal of Power Sources, vol. 275, p. 429–434, 2015.

[24] S. J. Harris and P. Lu, “Effects of inhomogeneities - nanoscale to mesoscale - on the durability of Li-ion batteries,” The Journal of Physical Chemistry C, vol. 117, no. 13, p. 6481–6492, 2013.

[25] M. M. Forouzan, B. A. Mazzeo, and D. R. Wheeler, “Modeling the effects of electrode microstructural heterogeneities on Li-ion battery performance and lifetime,” Journal of The Electrochemical Society, vol. 165, no. 10, p. A2127–A2144, 2018.

[26] D. Kehrwald, P. R. Shearing, N. P. Brandon, P. K. Sinha, and S. J. Harris, "Local tortuosity inhomogeneities in a lithium battery composite electrode," Journal of The Electrochemical Society, vol. 158, no. 12, p. A1393, 2011.

[27] L. Cai, K. An, Z. Feng, C. Liang, and S. J. Harris, "In-situ observation of inhomogeneous degradation in large format Li-ion cells by neutron diffraction," Journal of Power Sources, vol. 236, p. 163–168, 2013.

[28] J. Cannarella and C. B. Arnold, "The effects of defects on localized plating in lithium-ion batteries," Journal of The Electrochemical Society, vol. 162, no. 7, p. A1365–A1373, 2015.

[29] J. E. Vogel, M. M. Forouzan, E. E. Hardy, S. T. Crawford, D. R. Wheeler, and B. A. Mazzeo, "Electrode microstructure controls localized electronic impedance in Li-ion batteries," Electrochimica Acta, vol. 297, p. 820–825, 2019.

[30] S. J. Harris, D. J. Harris, and C. Li, "Failure statistics for commercial lithium ion batteries: A study of 24 pouch cells," Journal of Power Sources, vol. 342, p. 589–597, 2017.

[31] B. Prifling, A. Ridder, A. Hilger, M. Osenberg, I. Manke, K. P. Birke, and V. Schmidt, "Analysis of structural and functional aging of electrodes in lithium-ion batteries during rapid charge and discharge rates using synchrotron tomography," Journal of Power Sources, vol. 443, p. 227259, 2019.

[32] B. Prifling, D. Westhoff, D. Schmidt, H. Markötter, I. Manke, V. Knoblauch, and V. Schmidt, "Parametric microstructure modeling of compressed cathode materials for Li-ion batteries," Computational Materials Science, vol. 169, p. 109083, 2019.

[33] D. Westhoff, I. Manke, and V. Schmidt, "Generation of virtual lithium-ion battery electrode microstructures based on spatial stochastic modeling," Computational Materials Science, vol. 151, p. 53–64, 2018.

[34] D. Westhoff, J. Feinauer, K. Kuchler, T. Mitsch, I. Manke, S. Hein, A. Latz, and V. Schmidt, "Parametric stochastic 3D model for the microstructure of anodes in lithium-ion power cells," Computational Materials Science, vol. 126, p. 453–467, 2017.

[35] J. Feinauer, T. Brereton, A. Spettl, M. Weber, I. Manke, and V. Schmidt, "Stochastic 3D modeling of the microstructure of lithium-ion battery anodes via Gaussian random fields on the sphere," Computational Materials Science, vol. 109, p. 137–146, 2015.

[36] D. Westhoff, J. Skibinski, O. Šedivý, B. Wysocki, T. Wejrzanowski, and V. Schmidt, "Investigation of the relationship between morphology and permeability for open-cell foams using virtual materials testing," Materials & Design, vol. 147, p. 1–10, 2018.

[37] O. Stenzel, O. M. Pecho, L. Holzer, M. Neumann, and V. Schmidt, "Predicting effective conductivities based on geometric microstructure characteristics," AIChE Journal, vol. 62, no. 5, p. 1834–1843, 2016.

[38] O. Stenzel, O. M. Pecho, L. Holzer, M. Neumann, and V. Schmidt, "Big data for microstructure-property relationships: A case study of predicting effective conductivities," AIChE Journal, vol. 63, no. 9, p. 4224–4232, 2017.

[39] M. Neumann, O. Stenzel, F. Willot, L. Holzer, and V. Schmidt, "Quantifying the influence of microstructure on effective conductivity and permeability: Virtual materials testing," International Journal of Solids and Structures, vol. 184, p. 211–220, 2020.

[40] G. Gaiselmann, M. Neumann, V. Schmidt, O. Pecho, T. Hocker, and L. Holzer, "Quantitative relationships between microstructure and effective transport properties based on virtual materials testing," AIChE Journal, vol. 60, no. 6, p. 1983–1999, 2014.

[41] D. Westhoff, J. J. van Franeker, T. Brereton, D. P. Kroese, R. A. J. Janssen, and V. Schmidt, "Stochastic modeling and predictive simulations for the microstructure of organic semiconductor films processed with different spin coating velocities," Modelling and Simulation in Materials Science and Engineering, vol. 23, no. 4, p. 045003, 2015.

[42] F. Wilde, M. Ogurreck, I. Greving, J. U. Hammel, F. Beckmann, A. Hipp, L. Lottermoser, I. Khokhriakov, P. Lytaev, T. Dose, H. Burmester, M. Müller, and A. Schreyer, "Micro-CT at the imaging beamline P05 at PETRA III," AIP Conference Proceedings, vol. 1741, no. 1, p. 030035, 2016.

[43] M. Ogurreck, F. Wilde, J. Herzen, F. Beckmann, V. Nazmov, J. Mohr, A. Haibel, M. Müller, and A. Schreyer, "The nanotomography endstation at the PETRA III imaging beamline," Journal of Physics: Conference Series, vol. 425, no. 18, p. 182002, 2013.

[44] W. van Aarle, W. J. Palenstijn, J. D. Beenhouwer, T. Altantzis, S. Bals, K. J. Batenburg, and J. Sijbers, "The ASTRA toolbox: A platform for advanced algorithm development in electron tomography," Ultramicroscopy, vol. 157, p. 35–47, 2015.

[45] W. van Aarle, W. J. Palenstijn, J. Cant, E. Janssens, F. Bleichrodt, A. Dabravolski, J. D. Beenhouwer, K. J. Batenburg, and J. Sijbers, "Fast and flexible X-ray tomography using the ASTRA toolbox," Optics Express, vol. 24, no. 22, p. 25129–25147, 2016.

[46] R. C. Gonzalez and R. E. Woods, Digital Image Processing. New Jersey: Prentice Hall, 3rd ed., 2008.

[47] I. Molchanov, Theory of Random Sets. London: Springer, 2005.

[48] S. N. Chiu, D. Stoyan, W. S. Kendall, and J. Mecke, Stochastic Geometry and its Applications. Chichester: J. Wiley & Sons, 3rd ed., 2013.

[49] K. Schladitz, J. Ohser, and W. Nagel, "Measuring intrinsic volumes in digital 3D images," in 13th International Conference Discrete Geometry for Computer Imagery (A. Kuba, L. Nyúl, and K. Palágyi, eds.), (Berlin), p. 247–258, Springer, 2007.

[50] M. B. Clennell, "Tortuosity: a guide through the maze," Geological Society, London, Special Publications, vol. 122, no. 1, p. 299–344, 1997.

[51] B. Ghanbarian, A. G. Hunt, R. P. Ewing, and M. Sahimi, “Tortuosity in porous media: a critical review,” Soil Science Society of America Journal, vol. 77, no. 5, p. 1461–1477, 2013.

[52] B. Tjaden, D. J. L. Brett, and P. R. Shearing, “Tortuosity in electrochemical devices: a review of calculation approaches,” International Materials Reviews, vol. 63, no. 2, p. 47–67, 2018.

[53] D. Jungnickel, Graphs, Networks and Algorithms. Algorithms and Computation in Mathematics, Berlin: Springer, 3rd ed., 2007.

[54] M. Neumann, C. Hirsch, J. Staněk, V. Beneš, and V. Schmidt, “Estimation of geodesic tortuosity and constrictivity in stationary random closed sets,” Scandinavian Journal of Statistics, vol. 46, no. 3, p. 848–884, 2019.

[55] G. Matheron, Random Sets and Integral Geometry. New York: J. Wiley & Sons, 1975.

[56] J. Serra, Image Analysis and Mathematical Morphology. London: Academic Press, 1982.

[57] J. Ohser and F. Mücklich, Statistical Analysis of Microstructures in Materials Science. Chichester: J. Wiley & Sons, 2000.

[58] J. Ohser and K. Schladitz, 3D Images of Materials Structures: Processing and Analysis. Weinheim: J. Wiley & Sons, 2009.

[59] S. Torquato, Random Heterogeneous Materials - Microstructure and Macroscopic Properties. New-York: Springer, 2002.

[60] B. Münch and L. Holzer, “Contradicting geometrical concepts in pore size analysis attained with electron microscopy and mercury intrusion,” Journal of the American Ceramic Society, vol. 91, no. 12, p. 4059–4067, 2008.

[61] L. Holzer, D. Wiedenmann, B. Münch, L. Keller, M. Prestat, P. Gasser, I. Robertson, and B. Grobéty, “The influence of constrictivity on the effective transport properties of porous layers in electrolysis and fuel cells,” Journal of Materials Science, vol. 48, p. 2934–2952, 2013.

[62] P. Soille, Morphological Image Analysis: Principles and Applications. New York: Springer, 2^{nd} ed., 2003.

[63] J. Hoshen and R. Kopelman, “Percolation and cluster distribution. I. Cluster multiple labeling technique and critical concentration algorithm,” Physical Review B, vol. 14, no. 8, p. 3438–3445, 1976.

[64] S. Cooper, A. Bertei, P. Shearing, J. Kilner, and N. Brandon, “TauFactor: An open-source application for calculating tortuosity factors from tomographic data,” SoftwareX, vol. 5, p. 203–210, 2016.

[65] C.-J. Bae, C. K. Erdonmez, J. W. Halloran, and Y.-M. Chiang, “Design of battery electrodes with dual-scale porosity to minimize tortuosity and maximize performance,” Advanced Materials, vol. 25, no. 9, p. 1254–1258, 2013.

[66] M. Doyle and J. Newman, "Comparison of modeling predictions with experimental data from plastic lithium ion cells," Journal of The Electrochemical Society, vol. 143, p. 1890, 1996.

[67] J. Newman and K. Thomas-Alyea, Electrochemical Systems. The ECS Series of Texts and Monographs, Hoboken: J. Wiley & Sons, 3rd ed., 2004.

[68] J. Landesfeind, J. Hattendorff, A. Ehrl, W. A. Wall, and H. A. Gasteigera, "Tortuosity determination of battery electrodes and separators by impedance spectroscopy," Journal of The Electrochemical Society, vol. 163, p. A1373, 2016.

[69] I. V. Thorat, D. E. Stephenson, N. A. Zacharias, K. Zaghib, J. N. Harb, and D. R. Wheeler, "Quantifying tortuosity in porous Li-ion battery materials," Journal of Power Sources, vol. 188, p. 592 – 600, 2009.

[70] T. Hutzenlaub, A. Asthana, J. Becker, D. Wheeler, R. Zengerle, and S. Thiele, "FIB/SEM-based calculation of tortuosity in a porous $\mathrm{LiCoO_2}$ cathode for a Li-ion battery," Electrochemistry Communications, vol. 27, p. 77–80, 2013.

[71] M. Neumann, E. Machado Charry, K. Zojer, and V. Schmidt, "On variability and interdependence of local porosity and local tortuosity in porous materials: a case study for sack paper," Methodology and Computing in Applied Probability, 2020. https://doi.org/10.1007/s11009-019-09761-1.

[72] R. Adler, The Geometry of Random Fields. Classics in Applied Mathematics, Philadelphia: Society for Industrial and Applied Mathematics, 2010.

[73] M. Armstrong, A. Galli, H. Beucher, G. Loc'h, D. Renard, B. Doligez, R. Eschard, and F. Geffroy, Plurigaussian Simulations in Geosciences. Berlin: Springer, 2nd ed., 2014.

[74] M. Neumann, M. Osenberg, A. Hilger, D. Franzen, T. Turek, I. Manke, and V. Schmidt, "On a pluri-Gaussian model for three-phase microstructures, with applications to 3D image data of gas-diffusion electrodes," Computational Materials Science, vol. 156, p. 325–331, 2019.

[75] B. Abdallah, F. Willot, and D. Jeulin, "Morphological modelling of three-phase microstructures of anode layers using sem images," Journal of Microscopy, vol. 263, no. 1, p. 51–63, 2016.

[76] M. Neumann, B. Abdallah, L. Holzer, F. Willot, and V. Schmidt, "Stochastic 3D modeling of three-phase microstructures for predicting transport properties: A case study," Transport in Porous Media, vol. 128, no. 1, p. 179–200, 2019.

[77] H. Moussaoui, J. Laurencin, Y. Gavet, G. Delette, M. Hubert, P. Cloetens, T. L. Bihan, and J. Debayle, "Stochastic geometrical modeling of solid oxide cells electrodes validated on 3D reconstructions," Computational Materials Science, vol. 143, p. 262–276, 2018.

[78] M. Neumann, S. Wetterauer, M. Osenberg, A. Hilger, A. Wagner, N. Bohn, J. Binder, I. Manke, T. Carraro, and V. Schmidt, "Stochastic microstructure modeling and numerical simulation of effective electronic conductivity of aggregated particles in hierarchically structured electrodes." Working paper (under preparation).

[79] D. Kroese, T. Taimre, and Z. Botev, Handbook of Monte Carlo Methods. Wiley Series in Probability and Statistics, Hoboken: J. Wiley & Sons, 2011.

[80] G. E. Forsythe, M. A. Malcolm, and C. B. Moler, Computer Methods for Mathematical Computations. Englewood Cliffs: Prentice Hall, 1976.

[81] R. Brent, Algorithms for Minimization without Derivatives. Dover Books on Mathematics, Mineola: Dover Publications, 2013.

[82] MATLAB, Version 9.4.0.813654 (R2018a). Natick, Massachusetts: The MathWorks Inc., 2018.

[83] T. F. Coleman and Y. Li, "On the convergence of interior-reflective Newton methods for nonlinear minimization subject to bounds," Mathematical Programming, vol. 67, p. 189–224, 1994.

[84] T. F. Coleman and Y. Li, "An interior trust region approach for nonlinear minimization subject to bounds," SIAM Journal on Optimization, vol. 6, no. 2, p. 418–445, 1996.

[85] C. Lantuejoul, Geostatistical Simulation: Models and Algorithms. Berlin: Springer, 2013.

[86] A. Lang and J. Potthoff, "Fast simulation of Gaussian random fields," Monte Carlo Methods and Applications, vol. 17, no. 3, p. 195–214, 2011.

[87] R. G. Regis and C. A. Shoemaker, "A stochastic radial basis function method for the global optimization of expensive functions," INFORMS Journal on Computing, vol. 19, p. 485–664, 2007.

[88] W. Burger and M. Burge, Digital Image Processing: An Algorithmic Introduction Using Java. London: Springer, 2^{nd} ed., 2016.

[89] T. Prill, D. Jeulin, F. Willot, J. Balach, and F. Soldera, "Prediction of effective properties of porous carbon electrodes from a parametric 3D random morphological model," Transport in Porous Media, vol. 120, no. 1, p. 141–165, 2017.